1166 Chem. Mater. **2002,** *14,* 1166−1173

Electrochemical Reactions of Iron Borates with Lithium: Electrochemical and in Situ Mössbauer and X-ray Absorption Studies

A. Ibarra-Palos,[†] C. Darie,[†] O. Proux,[†] J. L. Hazemann,[†] L. Aldon,[‡] J. C. Jumas,[‡]
M. Morcrette,[§] and P. Strobel*[,†]

Laboratoire de Cristallographie, CNRS, BP 166, 38042 Grenoble Cedex 9, France, and
Laboratoire des Agrégats Moléculaires et Matériaux Inorganiques (UMR 5072 CNRS),
Université Montpellier II, Place E. Bataillon, 34095 Montpellier Cedex 5, and
Laboratoire de Réactivité et Chimie des Solides, Université de Picardie Jules Verne,
80039 Amiens Cedex, France

Received August 3, 2001. Revised Manuscript Received November 26, 2001

Upon electrochemical reduction in a lithium cell, crystalline $FeBO_3$ and Fe_3BO_6 give amorphous compounds, which can be cycled reversibly at low potential (Rowsell, J. *Power Sources* **2001**, *97−98*, 254). We report here capacities as high as 300 Ah/kg at the 14th cycle. The mechanism of reaction was investigated by step-potential electrochemical spectroscopy and in situ Mössbauer and X-ray absorption spectroscopies on electrochemical cells encapsulated in thin sealed plastic bags. These techniques confirm the reduction mechanism consisting of the early destruction of the crystallized borates and a direct $Fe^{III}-Fe^0$ multiphase reduction on first discharge. On recharge and subsequent cyclings, a reversible redox reaction occurs between Fe^0 and $Fe^{II/III}$ in an amorphous or nanocrystalline matrix.

1. Introduction

Iron compounds have found little use in electrochemical energy storage so far, despite the low cost and environment-friendly character of iron, and the most prominent cathode materials for lithium batteries to date are oxidic compounds of manganese, cobalt, or nickel.[1] The use of iron is beset by the rather low potential of the Fe^{3+}/Fe^{2+} redox couple. However, this situation may change rapidly since the discovery of the covalency effect in oxoanionic compounds of iron,[2,3] and at least one iron compound, olivine-type $LiFePO_4$, yields a very stable charge−discharge behavior with a potential >3 V vs lithium.[4]

In a search for iron compounds with low molar mass (in order to reach a high mass capacity), we undertook an investigation of the lithium intercalation properties of iron(III) borates. The known crystallized phases, $FeBO_3$ with calcite structure[5] and Fe_3BO_6 with norbergite structure,[6] are not good candidates a priori for lithium intercalation because they do not possess open structures. When these compounds are reduced in a lithium electrochemical cell, however, Rowsell et al.[7] and our group[8] recently showed that these compounds undergo amorphization, yielding disordered phases that can be cycled with high reversibility at low potential. These materials apppear then as potential candidates for anodes in lithium reversible batteries. In this paper, we will focus on the in situ characterization of the cycling amorphous materials, using X-ray absorption and Mössbauer spectroscopies. Finally, it is worth noting that both $FeBO_3$ and Fe_3BO_6 are antiferromagnets with Néel temperatures above room temperature (348 and 508 K, respectively[9,10]) and are expected to give sextuplets in Mössbauer spectroscopy at room temperature.

2. Experimental Section

Synthesis and Characterization. Iron borates can be prepared by solid-state reaction between Fe_2O_3 and H_3BO_3.[11] However, the synthesis of $FeBO_3$ is not as straightforward as it may seem: an excess of boric acid is required to avoid unreacted iron oxide impurities in the final product, and the firing temperature range is limited by the decomposition into more thermally stable Fe_3BO_6 above ca. 900 °C.[11] Improvements of this solid-state procedure will be described in section 3.1.

Samples were characterized by X-ray diffraction using a Siemens D-5000 diffractometer equipped with Cu Kα radiation. Lattice constants were obtained by a least-squares refinement procedure including sample displacement correction (CELREF program).

Electrochemical Studies. Electrochemical tests were carried out in Swagelok cells vs lithium metal, using positive

---

* Corresponding author. E-mail: strobel@polycnrs-gre.fr.
[†] CNRS.
[‡] Université Montpellier II.
[§] Université de Picardie Jules Verne.

[1] Broussely, M.; Biensan, P.; Simon, B. *Electrochim. Acta* **1999**, *45*, 3−22.

[2] Padhi, A. K.; Nanjundaswamy, K. S.; Masquelier, C.; Okada, S.; Goodenough, J. B. *J. Electrochem. Soc.* **1997**, *144*, 1609−1613.

[3] Masquelier, C.; Padhi, A. K.; Nanjundaswamy, K. S.; Okada, S.; Goodenough, J. B. *J. Solid State Chem.* **1998**, *135*, 228−234.

[4] Yamada, A.; Chung, S. C.; Hinokuma, K. *J. Electrochem. Soc.* **2001**, *148*, A224−229.

[5] Diehl, R. *Solid State Commun.* **1974**, *17*, 743−745.

[6] Diehl, R.; Brandt, G. *Acta Crystallogr. B* **1975**, *31*, 1662−1664.

[7] Rowsell, T. J.; Gaubicher, T.; Nazar, L. F. *J. Power Sources* **2001**, *97−98*, 254−257.

[8] Ibarra Palos, A.; Morcrette, M.; Strobel, P. *J. Solid State Electrochem.* **2002**, *6*, 134−138.

[9] Pernet, M.; Elmaleh, D.; Joubert, J. C. *Solid State Commun.* **1970**, *8*, 1583−1587.

[10] Kovalenko, P. P.; Labushkin, V. G.; Sarkisov, E. R.; Tolpekin, I. G. *Sov. Phys. Solid State* **1987**, *29*, 340−341.

[11] Joubert, J. C.; Shirk, T.; White, W. B.; Roy, R. *Mater. Res. Bull.* **1968**, *3*, 671−678.

10.1021/cm010694q CCC: $22.00

pellets made from active material, carbon, and poly(tetrafluoroethylene) (PTFE) binder as described previously.[8] The electrolyte was a 1 M solution of $LiPF_6$ in EC−DMC (1:2). The cells were assembled in a glovebox under argon with 1 ppm H_2O. For spectroscopic studies, all-plastic cells were assembled using the Bellcore technique.[12] Electrochemical studies were carried out using a MacPile controller (Bio-Logic, Claix, France), in either galvanostatic mode or step-potential electrochemical spectroscopy (SPES),[21] using typically 10 mV/h steps. All electrochemical tests were carried out at room temperature. X-ray powder diagrams were also recorded on positive pellets after disassembling cells stopped at specific points of the cycling curves.

Mössbauer Spectroscopy. ^{57}Fe Mössbauer spectra were collected at room temperature on a EG&G constant accelerator spectrometer in transmission mode. The source of nominal activity of 10 mCi was ^{57}Co in a Rh matrix. The velocity scale was calibrated by using the standard magnetic sextuplet spectrum of a high-purity iron foil absorber. The origin of the isomer shift scale was determined from the center of the a-Fe spectrum also recorded at room temperature. Measurements were performed in situ, with flat plastic batteries as absorbers. Experimental data were analyzed using Ruebenbauer and Birshall's software by fitting the recorded spectra to Lorentzian profiles by the least-squares method.[13] The goodness of fit was controlled by the classical χ^2 test.

X-ray Absorption Spectroscopy. X-ray absorption spectroscopy was carried out on the IF beamline located on the BM32 bending magnet source of the European Synchrotron Radiation Facility (Grenoble, France). A two-crystal Si(111) monochromator was used. The dynamic bending of the second crystal allowed one to focalize the beam in the horizontal plane without flux loss. The spot size on the sample was around 300 × 300 μm^2. The intensities of the incident and transmitted beams were determined with silicon diodes.

For in situ measurements, samples were enclosed in flat plastic batteries centered with a homemade plastic sample holder and studied in transmission mode.[14] Calibration was achieved using an iron foil and pellets of $Fe^{III}BO_3$ and iron(II) oxalate diluted in BN in order to provide adequate transmittance. The metallic Fe reference foil was used together with all in situ samples to provide accurate energy calibration.

EXAFS oscillations $\chi(k)$ were extracted from the raw data using the SEDEM program.[15] All of the analyses were performed with the $k^2\chi(k)$ signals. The Fourier transform (FT) of the $k^2\chi(k)$ signal allows one to select peaks coming from each shell around the central absorbing atom in the pseudo radial distribution function. Filtering of the first shell, containing the Fe−O contributions, was done by inverse FT. The fitting procedure was performed on the filtered $k^2\chi(k)$ signals with the SEDEM program. Backscattering phase and amplitude values were taken from McKale et al.[16] The refinement quality was quantified via the residual factor R_f defined in ref 15.

For both Mössbauer and X-ray absorption spectroscopies, data were recorded during relaxation of the electrochemical cell after partial discharge or charge to a given state, as detailed in section 3.3.

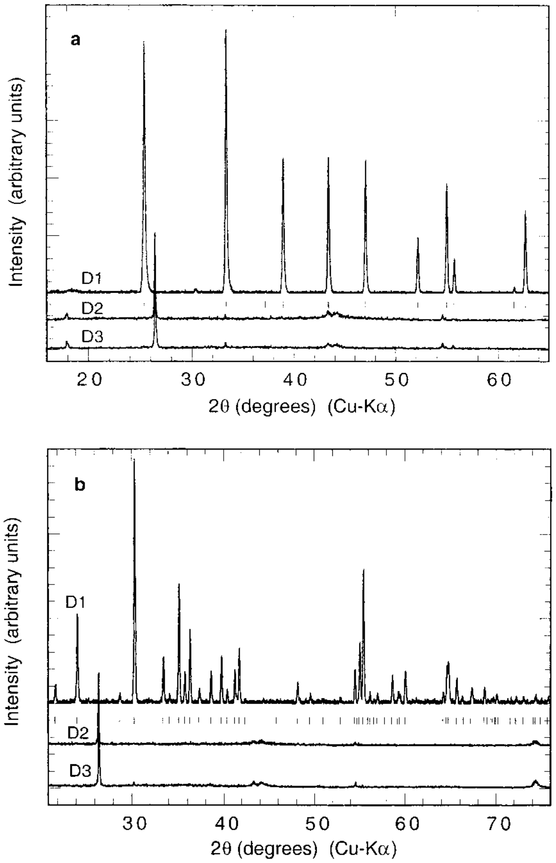

Figure 1. X-ray powder diagrams of pristine and cycled $FeBO_3$ (a) and Fe_3BO_6 (b). Bars show the main reflections of the known phases from JCPDS card nos. 76-701 (a) and 73-1385 (b). Symbols refer to electrochemical cells stopped at specific charge−discharge levels as shown in Figure 6. The 26.5° peak is due to graphite added in the oxide electrode pellet.

3. Results and Discussion

3.1. Iron Borate Synthesis. Our early attempts to prepare $FeBO_3$ invariably yielded products containing as much as 8% Fe_2O_3.[8] While this impurity did not have a significant effect on electrochemical performances, we modified the synthesis procedure to avoid the presence of Fe_2O_3 in the reaction medium, using iron(II) oxalate as a starting reagent. This precursor is advantageous because its decomposition at low temperature makes it very reactive toward boric acid. The synthesis of $FeBO_3$ was carried out from a 30% boric acid rich mixture at 700 °C. An oxygen flow was used to favor the Fe^{III} oxidation state in the reaction medium.

Fe_3BO_6 was prepared from the same reagents, with a 50% excess boric acid with respect to stoichiometry. It was found to decompose at ≈950 °C and was obtained iron oxide free after three firings at 925 °C with intermediate grinding and pelletizing.

All samples were washed with hot distilled water to eliminate any excess boric acid.

The X-ray powder patterns of the resulting powders (see Figure 1a,b, top diagrams) are consistent with literature data (JCPDS cards 76-701 and 73-1385). Refined lattice constants (in Å) are for $FeBO_3$ (rhom-

---

(12) Tarascon, J. M.; Gozdz, A. S.; Schmutz, C.; Shokoohi, F.; Warren, P. C. *Solid State Ionics* **1996**, *86*−*88*, 49−54.

(13) Ruebenbauer K.; Birshall, T. *Hyperfine Interact.* **1979**, *7*, 125−132.

(14) Ibarra Palos, A.; Strobel, P.; Proux, O.; Hazemann, J. L.; Anne, M.; Morcrette, M. *Electrochim. Acta* **2001**, in press.

(15) Aberdam, D. *J. Synchrotron Radiat.* **1998**, *5*, 1287−1293.

(16) McKale, A. G.; Veal, B. W.; Paulikas, A. P.; Chan, S. K.; Knapp, G. S. *J. Am. Chem. Soc.* **1988**, *110*, 3763.

(17) Chabre, Y. In C*hemical Physics of Intercalation*; Bernier, P., Ed.; Plenum Press: New York, 1993; p 129.

(18) Poizot, P.; Laruelle, S.; Grugeon, S.; Dupont, L.; Tarascon, J. M. *Nature* **2000**, *407*, 496−499; *C. R. Acad. Sci. Paris, Sér. IIc* **2000**, *3*, 681−691.

(19) Wilke, M.; Farges, F.; Petit, P. E.; Brown, G. E.; Martin, F. *Amer. Mineral.* **2001**, *86*, 714−730 and references therein.

(20) Briois, V.; Cartier, C.; Momenteau, M.; Maillard, P.; Zarembowitch, J.; Dartyge, E.; Fontaine, A.; Tourillon, G.; Thuéry, P.; Verdaguer, M. *J. Chim Phys.* **1989**, *86*, 1623.

(21) Thompson, A. H. *J. Electrochem. Soc.* **1979**, *126*, 608−616.

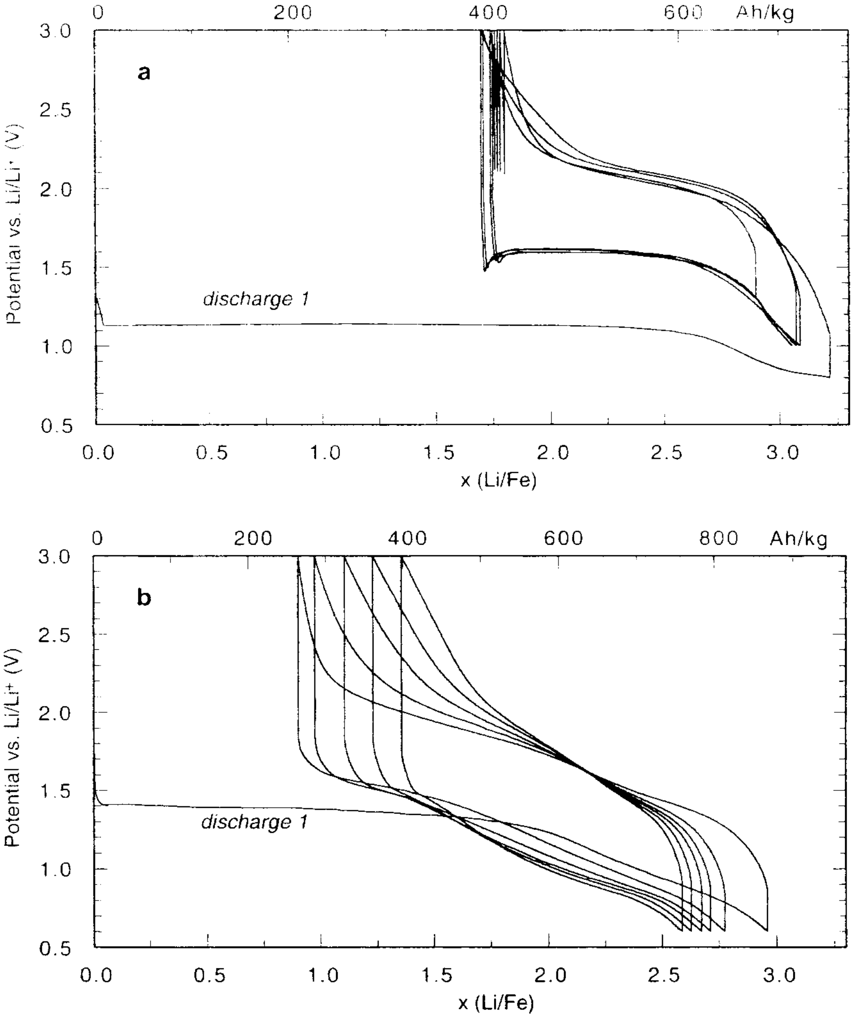

Figure 2. Typical charge−discharge curves of iron borate−lithium batteries in galvanostatic mode at room temperature: (a) $FeBO_3$ [25 mA·cm^{-2}, C/20 rate]; (b) Fe_3BO_6 [20 mA·cm^{-2}, C/30 rate].

bohedral, $R\bar{3}c$ space group) $a = 4.624(1)$ and $c = 14.481(3)$ and for Fe_3BO_6 (orthorhombic, *Pnma*) $a = 10.043(2)$, $b = 8.528(2)$, and $c = 4.460(2)$.

3.2. Electrochemical Behavior in Lithium Cells. The electrochemical behavior of $FeBO_3$ has been described previously.[7,8] Galvanostatic cycling curves and SPES curves of $FeBO_3$ and Fe_3BO_6 are shown in Figures 2 and 3, respectively. Throughout this paper, lithium contents x_{Li} will be expressed with respect to formulas containing one iron atom, i.e., $FeB_{1/3}O_2$ rather than Fe_3BO_6 in order to make comparisons easier.

The general trends of the electrochemical redox chemistry of $FeBO_3$ and Fe_3BO_6 in lithium cells are fairly similar. The first discharge gives rise to a long potential plateau extending to 3Li/Fe, i.e., to complete reduction to metallic iron. Rather surprisingly, in neither case is any specific step observed on passing at the Fe^{II} stage ($x = 1$ in Figure 2a,b). On charge, the behavior is completely different in potential E (higher), curve shape (S-shaped), and capacity (smaller). Figure 2 shows that both systems seem to allow stable cycling on a new electrochemical system formed in situ during the first discharge.

The sharp, irreversible peak in $i(U)$ on first discharge (Figure 3), corresponding to a very flat shape of $E(x)$, is typical of a two-phase reaction. This was confirmed by a discharge carried out using the potentiostatic intermittent titration technique with 10 mV potential steps on $FeBO_3$ (see Figure 4). The bell-shaped current response at the precise 1.20 V step is characteristic of a two-phase (or multiphase) system where the kinetics are controlled by the advance of the second-phase front.[17,18]

There are, however, significant differences between the two borates:

(i) The first discharge occurs at different potentials E (1.20 V for $FeBO_3$ and 1.42 V for Fe_3BO_6); in the latter case, the $E(x)$ plateau shows a break with a different slope at $x = 2$, while the $FeBO_3$ reduction reaction proceeds at 1.20 ± 0.01 V up to $x = 2.6$ (Figures 2 and 3). These results are in excellent agreement with those of Rowsell et al.[7]

(ii) While the charge−discharge polarization on further cycling has a comparable magnitude in both compounds, the potentials from the first charge onward are significantly higher in the $FeBO_3$ case (i.e., a situation opposite to that of the first discharge). This is illustrated by the important potential shift between the first discharge and the following ones for $FeBO_3$, while all discharges occur at the same potential for Fe_3BO_6 (see Figure 2). The $E(x)$ curves also have larger slopes in the latter case. This can be ascribed to differences in the reaction medium: boron contents are different, and the Mössbauer features of the Fe^0 species formed on first

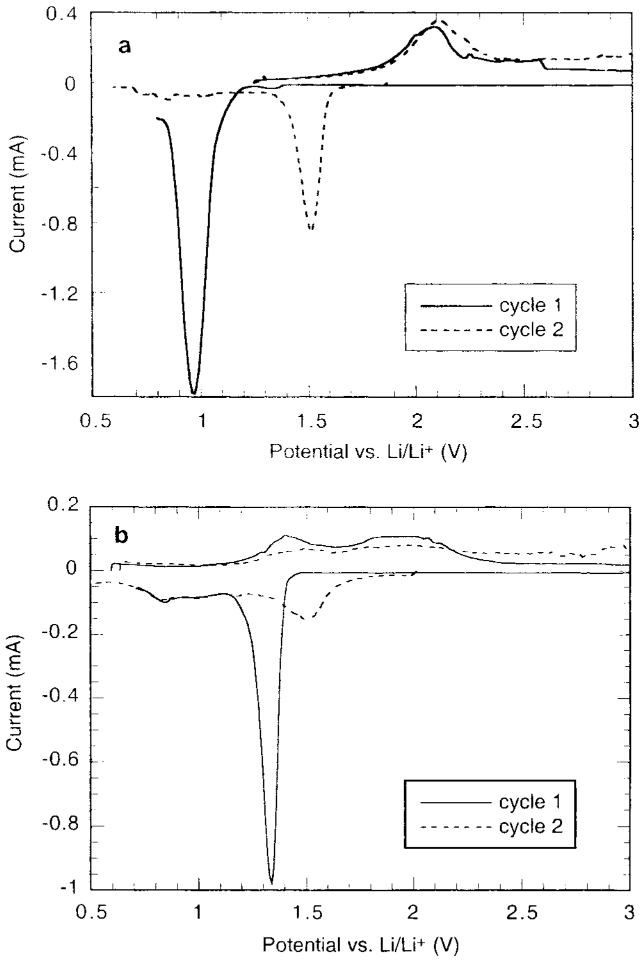

Figure 3. Step-potential voltammograms of iron borate−lithium batteries at 10 mV/h (first two cycles shown): (a) $FeBO_3$; (b) Fe_3BO_6.

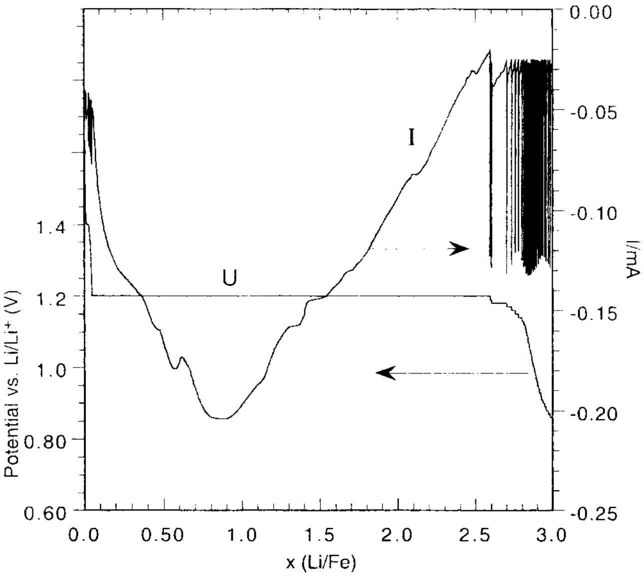

Figure 4. First discharge of $FeBO_3$ vs lithium metal under step-scanning potentiostatic control. The steps are 10 mV with a lower current limit of 25 μA.

discharge also show significant differences, especially in isomer shift (see section 3.4).

(iii) The reversible capacity Q is larger for $FeB_{1/3}O_2$ in the first 6−8 cycles. Note that when specific capacities are dealt with (i.e., per unit of active material mass), this compound is favored over $FeBO_3$ because of its smaller molar mass per iron atom (compare top x scales in Figure 2a,b). Reversible capacities are plotted as a function of the cycle number in Figure 5. While they tend to decrease significantly on cycling, they remain quite high (ca. 300 mAh/g) compared to that of the most-used cathode material in lithium batteries so far, $LiCoO_2$ (140 mAh/g). However, the low potentials of iron borate redox reactions vs Li/Li^+ makes them rather possible *anodic* materials for lithium-ion batteries. Note that the difference in capacity of Fe_3BO_6 and $FeBO_3$ levels out after about 10 cycles. The capacities obtained here (250 mAh/g at the 12th cycle) are higher than those reported recently by Rowsell et al.[7] for samples prepared by a similar solid-state reaction. These authors, however, showed that the capacity retention of Fe_3BO_6 is considerably increased when the material is synthesized at 700 °C from lyophilized, nanoparticulate Fe_2O_3. Such differences illustrate the key role of the particle size in the cyclability of oxidic electrode materials.

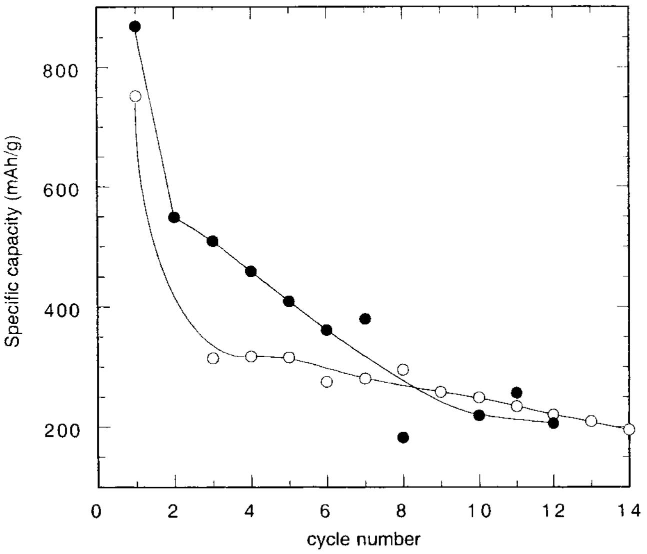

Figure 5. Evolution of the specific capacity of iron borate−lithium batteries at ca. C/20 rate in the voltage window 0.6−3.0 V vs Li/Li^+: ○, $FeBO_3$; ●, Fe_3BO_6.

Higher capacities at low potential have also been achieved recently on simple transition-metal binary oxides such as CoO.[18] The electrochemical behavior of iron borate systems resembles that of the binary oxides, especially in the occurrence of a long, flat first-discharge plateau at low potential followed by cycling on a different, higher-potential system. However, we checked that the redox behavior of $FeBO_3$ is different from that of Fe_2O_3, in terms of both potential and cyclability.[8]

3.3. Structural Characterization on Discharged/Recharged Cells. To better characterize the redox system formed in situ during the first discharge, cells in various states of discharge were disassembled and the positive pellets examined by X-ray powder diffraction. In addition, in situ measurements on plastic batteries (without disassembling) were performed in Mössbauer and X-ray absorption spectroscopies. Spectra were recorded at selected positions of the studied systems along the discharge−charge curve. These positions are indicated in Figure 6 (points D, M, and A for X-ray diffraction, Mössbauer spectroscopy, and X-ray absorption, respectively).

Table 1. Experimental Parameters of Mössbauer Spectra of Li_xFeBO_3 at Various States of Charge−Discharge[a]

x	δ_{IS} (mm/s)	Δ_{QS} (mm/s)	Γ (mm/s)	$H(T)$	RA (%)	attribution	charge Mössbauer	charge electrochemical
0	0.392(1)	0.18(4)	0.246(2)	34.2(1)	100	Fe^{III}	3	3
1.1 (discharge)	0.39(2)	0.18(4)	0.27(4)	34.0(1)	49.4	Fe^{III}	1.95	1.90
	0.32(1)	0.74(1)	0.61(4)		15.2	Fe^{III}		
	0.0	0.57	0.61(4)		35.3	Fe^0		
2.78 (discharge)	−0.15(1)	0.49(1)	0.35		45.0	Fe^0	0	0.2
	0.169(2)	0.687(4)	0.35		55.0	Fe^0		
2.13 (recharge)	−0.10(1)	0.39(2)	0.53		71.0	Fe^0	0.6	0.9
	1.45(4)	1.13(6)	0.53		29.0	Fe^{II}	Fe^{II}	

[a] δ_{IS} = isomer shift, Δ_{QS} = quadrupole splitting, Γ = full width at half-maximum, $H(T)$ = magnetic field, RA = relative area.

Table 2. Experimental Parameters of Mössbauer Spectra of $Li_xFeB_{1/3}O_2$ at Various States of Charge−Discharge (Symbols as in Table 1)

x	δ_{IS} (mm/s)	Δ_{QS} (mm/s)	Γ (mm/s)	$H(T)$	RA (%)	attribution	charge Mössbauer	charge electrochemical
0	0.373(1)	0.28(1)	0.253(1)	42.6(1)	65	Fe^{III}	3	3
	0.386(2)	0.120(4)		45.6(1)	35	Fe^{III}		
1.1 (discharge)	0.370(2)	0.276(1)	0.485(1)	42.4(1)	29.9	Fe^{III}	2.4	1.9
	0.388(2)	0.103(4)		45.4(1)	16.0	Fe^{III}		
	0.333(1)	0.944(1)			33.8	Fe^{III}		
	0.097(2)	0.36(4)			20.3	Fe^0		
2.74 (discharge)	−0.26(5)	0.73(6)	0.67(4)		39.0	Fe^0	0	0.26
	0.22(4)				61.0	Fe^0		
0.9 (recharge)	0.85(5)	1.6(1)	0.58(5)		31.0	Fe^{II}	2.7	2.1
	0.29(2)	0.82(2)			69.0	Fe^{III}		

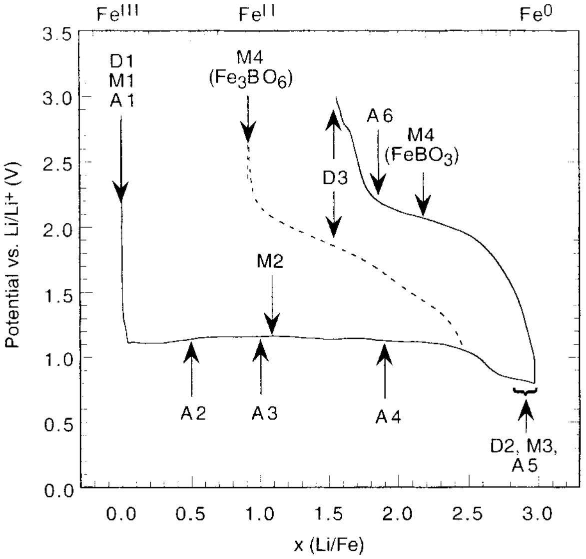

Figure 6. Typical first discharge−charge curve of iron borates, showing the compositions where in situ Mössbauer spectra (M points) and X-ray absorption (A points, $FeBO_3$ only) and ex situ X-ray diffraction patterns (D points) were recorded. For clarity, separate curves are shown for charge only ($FeBO_3$, full line; Fe_3BO_6, broken line).

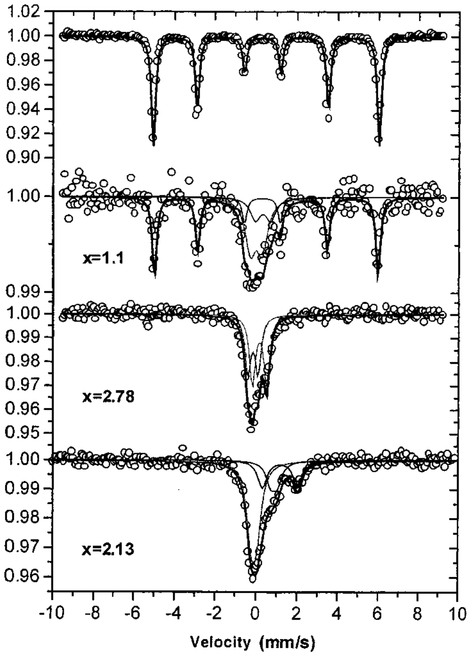

Figure 7. Mössbauer spectra of $FeBO_3$ recorded at points M1 (top) to M4 (bottom) as defined in Figure 6.

X-ray diffraction was recorded on $FeBO_3$ and Fe_3BO_6 after the first discharge and the first charge. In all cases, it showed the absence of any remaining crystallized phase (see Figure 1a,b, lower part). Thus, both borates undergo a phase transformation on the first discharge and cycle on stable, amorphous phases. This is consistent with the fact that the initial structures of $FeBO_3$ (calcite[5]) and Fe_3BO_6 (norbergite[6]) do not allow topotactic intercalation of lithium.

3.4. Mössbauer Spectroscopy. Mössbauer spectra were recorded at room temperature at different stages of charge or discharge as indicated in Figure 6 (points M). The refined hyperfine parameters are summarized in Tables 1 and 2. Pristine $FeBO_3$ and Fe_3BO_6 give very typical Mössbauer spectra including one or two Fe^{III} sextuplets with magnetic fields of 34.2 and 42.6−45.6 T, respectively (see Figures 7 and 8, top). These spectra are in complete agreement with the crystal structures which contain one octahedral iron site in FeBO[5,7] and two iron sites (in much more distorted octahedral coordination) in Fe_3BO_6.[6]

Point M2 was included to check for a possible Fe^{II} stage during electrochemical reduction on discharge. However, in neither the $FeBO_3$ nor the Fe_3BO_6 case was any Fe^{II} feature seen; instead, both systems became multiphase with the coexistence of a remaining fraction of unreacted borate, another new noncrystalline, nonmagnetic Fe^{III} phase A, and an Fe^0 component. So, a possible reaction mechanism on electrochemical reduction is

$$Fe^{III}{-}B{-}O(\text{cryst.}) + xe^- \rightarrow (1-x/3)Fe^{III}_{\text{Anc}} + x/3Fe^0_{\text{nc}} + Li{-}B{-}O_{\text{nc}}$$

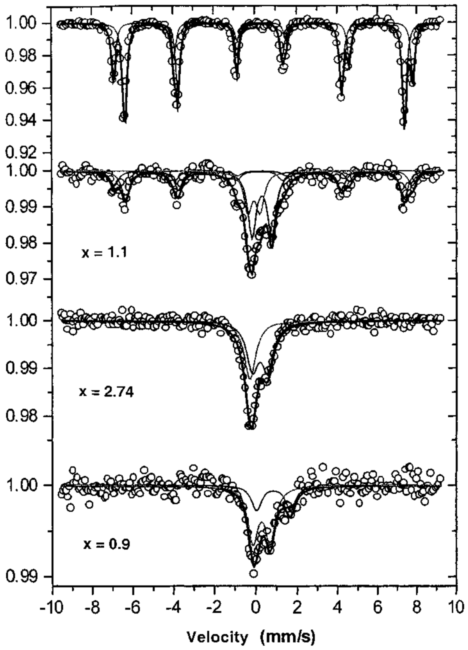

Figure 8. Mössbauer spectra of Fe_3BO_6 recorded at points M1 (top) to M4 (bottom) as defined in Figure 6.

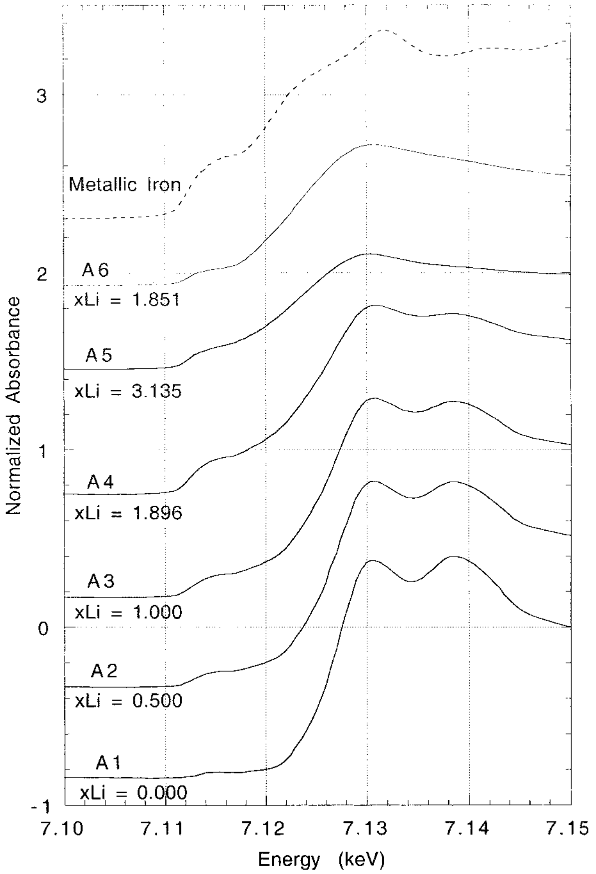

Figure 9. XANES spectra at the iron K edge of $FeBO_3$ for different states of electrochemical reduction in a lithium battery.

where the subscript nc indicates that the phases formed in situ are nano- or noncrystalline.

The Mössbauer spectrum analysis for composition $Li_{1.1}FeBO_3$ gives an average iron oxidation state of 1.95, in excellent agreement with that obtained from electrochemistry ($Fe^{1.90+}$). The agreement is poorer in the $Li_{1.1}FeB_{1/3}O_2$ case (see Table 2). This can be due to the difference between formal and effective charges on iron atoms. In fact, the Mössbauer absorption depends on the Lamb–Mössbauer factor (or *f* factor), which is larger if the bond is more covalent (more rigid) at constant temperature. The overestimated value found for the iron oxidation state in $Li_{1.1}FeB_{1/3}O_2$ can be due to a higher degree of covalency in this compound.

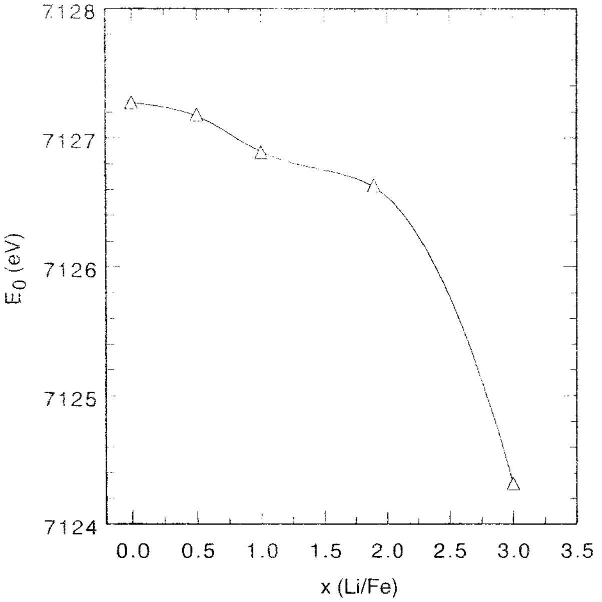

Figure 10. Fe K edge energy evolution with discharge in an $FeBO_3$–Li battery.

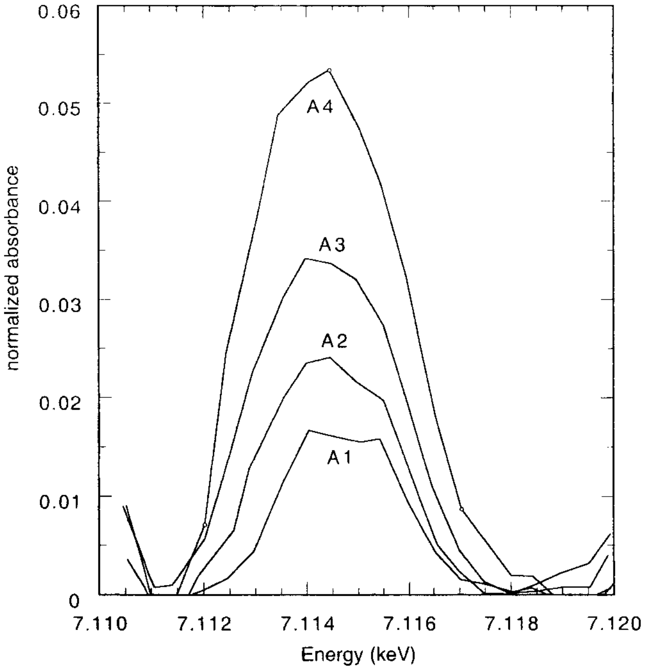

Figure 11. Enlarged view of the preedge peak of $FeBO_3$ at 7.114 keV as a function of discharge (see Figure 6 for sample nomenclature).

At the end of the first discharge (point M3 in Figure 6), only Fe^0 is seen, in agreement with a full discharge to metallic iron. The multiphase reaction evidence from electrochemical analysis (Figure 4) and reduction to metallic iron are thus confirmed. Note that in both cases the end product contains two different Fe^0 species, one

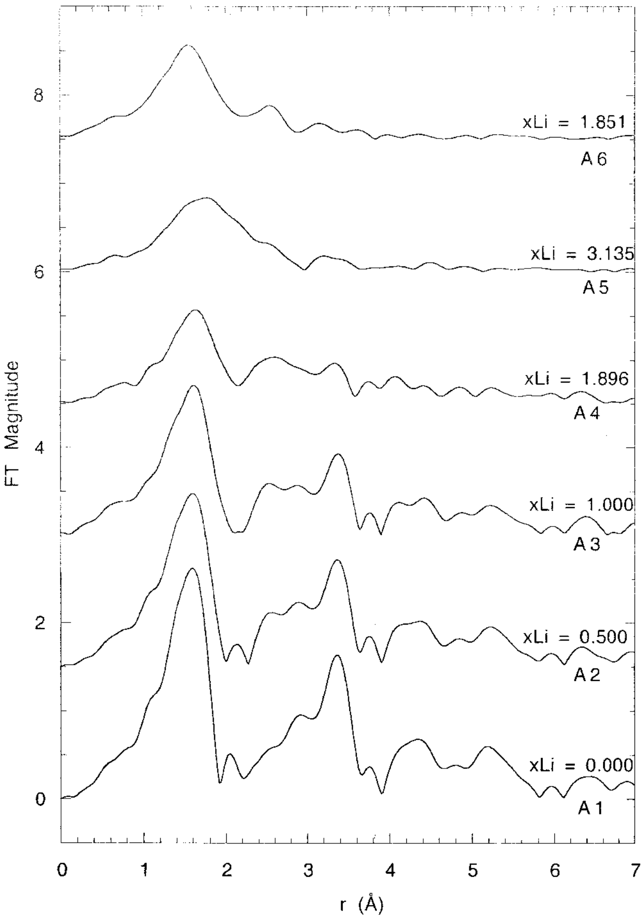

Figure 12. Fourier transforms of k^2-weighted Fe K edge EXAFS spectra of $FeBO_3$ as a function of the degree of reduction in a lithium battery.

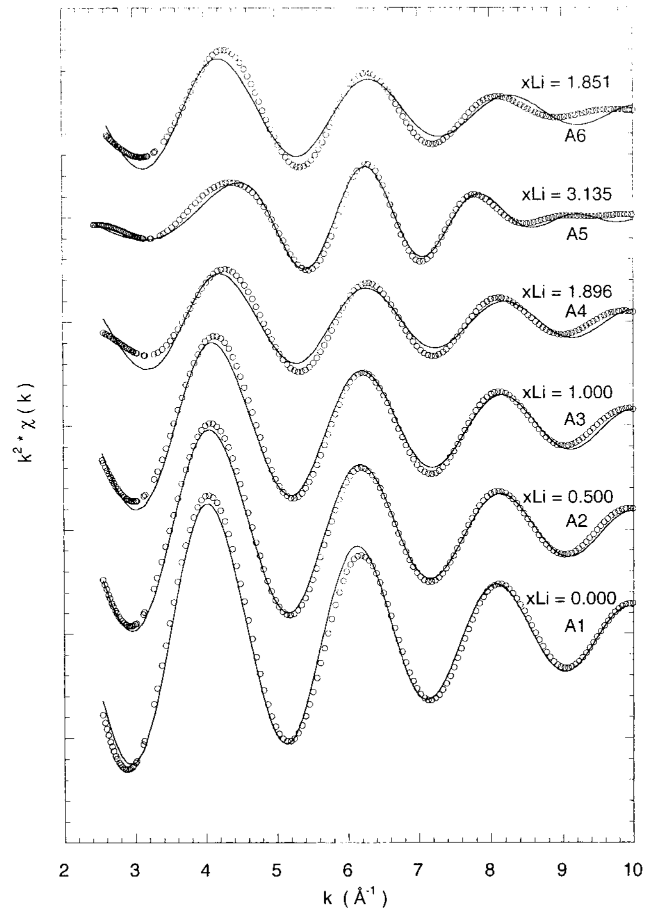

Figure 13. Filtered first-shell $k^2\chi(k)$ Fe K edge EXAFS spectra of $FeBO_3$ for different states of electrochemical reduction in a lithium battery. Filtering windows are given in Table 3.

with a positive isomer shift and one with a negative isomer shift.

On charge (point M4), the batteries used for in situ Mössbauer spectroscopy measurements behaved rather differently: while $FeBO_3$ was recharged only up to $x = 2.13$, Fe_3BO_6 could be recharged all the way to $x = 0.9$. In the battery stopped at $x = 2.13$ (i.e., formal iron oxidation state of 0.9), a mixture of Fe^0 and Fe^{II} is observed. In that recharged all the way to $x = 0.9$ (Fe_3BO_6 case), the Mössbauer spectrum can be fit with two Fe^{III} components. The Fe^{III} species formed in situ on recharge are quite different from the initial Fe_3BO_6, with no magnetic ordering detected at room temperature.

Similarly, the $FeBO_3$ recharge yields an Fe^{II} component, which was not found in the first discharge. These results thus fully confirm the conclusions of electrochemical studies, which pointed out (i) a dramatic structural change on first discharge and (ii) further cycling involving redox reactions of iron in amorphous oxide or borate systems.

3.5. X-ray Absorption. This technique was applied to $FeBO_3$ only, in an in situ configuration in discharge (see data points A in Figure 6). Because of the time constraints of the synchrotron line, the plastic battery used in this experiment was discharged using capacity steps corresponding to $\Delta x(\mathrm{Li/Fe}) = 1$ per hour and then relaxed during XAS acquisition (three successive scans, i.e., ca. 1.75 h acquisition time for each composition point). Perhaps because of this rather high discharge rate, this cell did not allow one to exceed $x = 2.37$ on the first discharge, and points A5 and A6 were recorded on other "fresh" batteries discharged simultaneously ex situ.

(a) XANES. The XANES spectra (see Figure 9) are characterized by a shape approaching that of metallic iron with increasing discharge. They contain a weak preedge peak at 7114 eV and a main, large peak, which are ascribed to 1s → 3d and 1s → 4p electronic transitions, respectively. As a consequence, the main peak energy depends on the energy of the 4p continuum, i.e., on the overlap of Fe and O orbitals, which, in turn, is related to the effective atomic charge of iron.[19] This dependence is best quantified as the position of the main peak inflection point, which is plotted against the reduction level in the lithium battery in Figure 10. A monotonic decrease is clearly seen, showing that iron is indeed reduced in the electrochemical process.

The preedge 1s → 3d transition is dipole-forbidden for purely centrosymmetric sites. For octahedral Fe−O coordination, as is the case in $FeBO_3$, it is expected to be weak but not totally absent, because there is always a partial hybridization between Fe 3d and O 2p states.[20] A detailed plot of the preedge after subtracting the background (Figure 11) shows a clear increase in the preedge peak intensity with discharge. This feature can be attributed to the appearance of a nonoctahedral Fe−O environment with reduction in the battery, in

Table 3. Curve-Fitting Results (First Shell) for the Fourier-Filtered $k^2\chi(k)$ Fe K Edge EXAFS of Li_xFeBO_3 at Various States of Charge−Discharge[a]

composition point (see Figure 5)	x	back-FT filtering window (Å)	R (Å)	σ^2 (Å^2)	CN	ΔE_0 (eV)	residual factor
A1	0.00	0.40−1.94	2.028[b]	0.0055(2)	6.0[b]	1.7(1)	0.017
A2	0.50	0.40−2.0	2.017(2)	0.0059(2)	4.63(5)	1.6(2)	0.011
A3	1.00	0.40−2.12	2.017(2)	0.0056(2)	3.80(6)	2.9(2)	0.021
A4	1.896	0.42−2.14	2.023(3)	0.0044(4)	2.13(6)	7.0(3)	0.078
A5 (ex situ)	3.135	0.40−3.0	2.011(6)	0.0050[c]	1.45(4)	4.9(7)	0.034
A6 (ex situ)	1.85	0.38−2.22	2.000(4)	0.0069(5)	2.5(7)	4.8(4)	0.070

[a] R = first-shell distance around Fe, σ = Debye−Waller factor, CN = coordination number around Fe atoms, ΔE_0 = energy threshold difference. [b] Fixed values from the known crystal structure of $FeBO_3$.[5] [c] Fixed (second-shell refinement attempt including Fe−Fe distance).

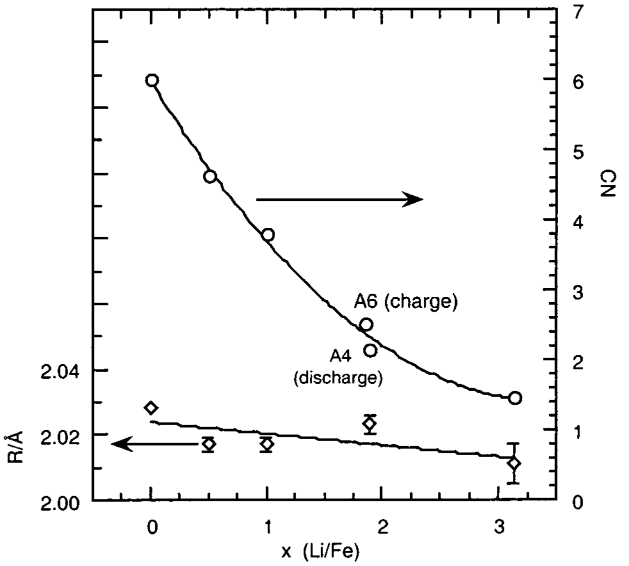

Figure 14. Evolution of Fe−O bond length R (diamonds) and Fe coordination number CN (circles) with the degree of reduction in a lithium battery.

agreement with a mechanism involving the destruction of the initial, crystallized phase $FeBO_3$.

(b) EXAFS. The evolution of radial distribution functions after Fourier transformation of $k^2\chi(k)$ weighted data is given in Figure 12. Starting from the bottom of this figure, the A1 spectrum (xLi = 0, i.e., pristine $FeBO_3$) shows a well-defined structure, with the first and second shells corresponding to Fe−O and Fe−Fe distances in the $FeBO_3$ structure, respectively.

As the battery is discharged (going up in Figure 12), a progressive decrease in amplitude of all components is observed. The smearing out of the structure indicates a wide distribution of distances between iron atoms and its neighbors. More remarkably, the expected large contributions of the Fe−Fe shell in samples containing high fractions of metallic iron do not show up. These results confirm the mechanism of destruction of the crystallized network of iron borate on reduction and give evidence of the formation of a particular form of iron in the fully discharged battery, perhaps as an intermetallic phase where iron is coordinated to light atoms such as lithium or boron. More insight on the nature of this Fe^0 species might be obtained using transmission electron microscopy.

The back-transform first-shell $k^2\chi$ function, with the corresponding fit, and numerical results are given in Figure 13 and Table 3, respectively. The fit quality is poorer for samples with $x \approx 2$ (see residual factor values in Table 3). The filtering window (see Table 3) was enlarged for sample A5 (close to Fe^0), in attempts to include Fe−Fe distances in the refinement.

The main results of this analysis are (i) an almost negligible change in Fe−O distances R ($2.011 \leq R \leq 2.028$ along a full discharge) and (ii) a dramatic decrease in oxygen neighbors number CN with increasing electrochemical reduction (see Figure 14). Regarding interatomic distances, it should be pointed out that an *increase* in R would be expected for the reduction $Fe^{III} \rightarrow Fe^{II}$. No such effect is seen, confirming the absence of any Fe^{II} stage in the reduction of $FeBO_3$ in a lithium battery. The CN of iron in the Fe−O shell, on the contrary, shows a very strong drop, from 6 in $FeBO_3$ to ca. 1.5 for the full reduction.

These results are fully consistent with the multiphase mechanism proposed above for the first discharge: the main Fe−O phase $FeBO_3$ does not intercalate lithium and keeps a fixed stoichiometry—hence the constant Fe−O distance. This phase is progressively depleted, yielding amorphous Fe^0 as the reduction reaction proceeds—hence a progressive decrease in the oxidized phase fraction in the reaction medium and the observed drop in CN. As expected from the depletion in Fe−O neighbors, the esd on distances, Debye−Waller factors, and the energy threshold increase significantly with in situ reduction of $FeBO_3$ (see Table 3).

4. Conclusions

Two iron(III) borates, $FeBO_3$ and Fe_3BO_6, were studied as electrodes for lithium batteries. Both materials undergo a dramatic structural change on first reduction, occurring at 1.20 and 1.42 V vs Li/Li, respectively. The initial specific capacities are high (>300 mAh/g), and the capacity retention can be much improved by optimizing the particle size.[7] The reaction mechanism was determined by a combination of electrochemical (potentiostatic) and in situ spectroscopic techniques (Mössbauer and X-ray absorption). The crystallized borates do not intercalate lithium but are progressively reduced into amorphous iron, without giving any definite Fe^{II} step; this highly divided iron can be cycled reversibly against lithium, at a slightly higher potential.

Acknowledgment. This work is part of the thesis of A. Ibarra-Palos, which is funded by a grant from the Mexican−French cooperation agreement CONACYT/SFERE. The authors thank Yvonne Soldo and Michel Anne for their assistance in X-ray absorption measurements.

CM010694Q